Journal of Advanced Ceramics
2022, **11**(11): 1735–1750
https://doi.org/10.1007/s40145-022-0644-9
ISSN 2226-4108
CN 10-1154/TQ

Research Article

Photo-assisted charging of carbon fiber paper-supported CeO_2/MnO_2 heterojunction and its long-lasting capacitance enhancement in dark

Weiyi YANG, Jian WANG, Shuang GAO, Haoyu ZHANG, Hongyang WANG, Qi LI*

Key Laboratory of Advanced Technologies of Materials (*Ministry of Education*), *School of Materials Science and Engineering*, *Southwest Jiaotong University*, *Chengdu 610031*, *China*

Received: July 7, 2022; Revised: August 3, 2022; Accepted: August 18, 2022

Abstract: It is important to develop green and sustainable approaches to enhance electrochemical charge storage efficiencies. Herein, a two-step *in-situ* growth process was developed to fabricate carbon fiber paper-supported CeO_2/MnO_2 composite (CeO_2/MnO_2–CFP) as a binder-free photo-electrode for the photo-assisted electrochemical charge storage. The formation of CeO_2/MnO_2 type II heterojunction largely enhanced the separation efficiency of photo-generated charge carriers, resulting in a substantially enhanced photo-assisted charging capability of ~20%. Furthermore, it retained a large part of its photo-enhanced capacitance (~56%) in dark even after the illumination was off for 12 h, which could be attributed to its slow release of stored photo-generated electrons from its specific band structure to avoid their reaction with O_2 in dark. This study proposed the design principles for supercapacitors with both the photo-assisted charging capability and its long-lasting retainment in dark, which may be readily applied to other pseudocapacitive materials to better utilize solar energy.

Keywords: supercapacitors; carbon fiber paper-supported CeO_2/MnO_2 heterojunction (CeO_2/MnO_2–CFP); photo-assisted charging; long-lasting effect in dark; slow release of stored electrons

1 Introduction

The rapid consumption of fossil fuels and the ensuing environmental pollution have led to increasing demands in developing sustainable energy supplies throughout the world [1–3]. Among various energy resources, solar energy is virtually unlimited and regarded as one of the most promising solutions to address these concerns [4–9]. However, solar energy is low-density and intermittent, which has to be stored to compensate the fluctuating availability of the Sun and the actual energy demand [6,10]. Supercapacitor is generally considered as one kind of the most important energy storage devices with the advantages of low cost, high power density, and long lifespan [8–10]. Despite these meritorious properties, supercapacitors suffer from relatively low energy densities when compared with conventional battery systems, which significantly impedes their applications [14,15].

Recently, energy storage devices with the photo-charging or photo-assisted charging capability have been developed to promote their electrochemical charge storage with the utilization of solar energy [16–26]. In these systems, photo-generated electrons and holes participated in their charging and discharging processes

* Corresponding author.
E-mail: qiliuiuc@swjtu.edu.cn

when these semiconductor-based active materials were illuminated to enhance their energy conversion and charge storage efficiencies. For example, a photo-rechargeable zinc ion battery was proposed using V_2O_5 as the photo-active cathodes, which showed a significant capacity increase under illumination, and its photo-conversion efficiencies reached ~1.2% [25]. An *et al*. [26] reported a nanopore Cu@Cu_2O hybrid array with an increased capacitance of ~37.9% under photo-assisted charging, which was attributed to photo-generated charge carriers. Furthermore, photo-assisted charging of zinc ion-based capacitors, batteries, as well as supercapacitors was also successively proposed and showed application potentials [17–27]. However, they generally lacked of the capability to retain their extra charge storages from the photo-assisted charging process when the illumination was switched off, which largely limited their practical applications.

Although MnO_2 has drawbacks of low actual specific capacitance and poor cycling stability due to its low conductivity and intrinsic redox reactions [28], it has emerged as a promising pseudocapacitive material among various active materials for supercapacitors owing to its high theoretical capacitance, low cost, environmental friendliness, and natural abundance [29,30], and has been attracting extensive research interests [31–35]. However, there is still no report in the literature on the photo-induced capacitance enhancement behavior of supercapacitors with traditional pseudocapacitive MnO_2-based materials as the active component, which may be related to the easy photo-generated charge carrier recombination in them to offset the photo-assisted charging effect. Due to their great application potentials, it is of great interest to develop strategies to endow the photo-assisted charging capability to MnO_2-based supercapacitors to enhance their capacitance. Furthermore, it would be even better if their capacitance enhancement by the photo-assisted charging could be retained in dark for an extended period of time.

Herein, we developed a two-step *in-situ* growth process to fabricate carbon fiber paper-supported CeO_2/MnO_2 composite (CeO_2/MnO_2–CFP) as a binder-free photoelectrode, which demonstrated a good photo-assisted charging capability and could retain a large part of its capacitance enhancement from the photo-assisted charging for an extended period of time in dark. CFP served as the support material for the growth of MnO_2, which could provide long-range electron-transport pathways, avoid the use of polymer binders, and effectively increase the contact area of the electrode. Subsequently, a small amount of CeO_2 nanoparticles were *in-situ* grown on the surface of MnO_2–CFP for the formation of CeO_2/MnO_2–CFP composite electrode. As a photosensitive semiconductor, CeO_2 has been extensively explored for a wide range of energy-related applications, including photocatalysis, supercapacitor, and lithium batteries [36–42]. The construction of a type II CeO_2/MnO_2 heterojunction could not only provide additional photo-induced charge carriers upon proper light irradiation in this material system, but also enhance the charge carrier separation in MnO_2 to make a better use of its photo-generated charge carriers to substantially promote its photo-assisted charging capability. Under visible light illumination, the as-prepared CeO_2/MnO_2–CFP electrode demonstrated a specific capacitance of ~303 $F \cdot g^{-1}$ at 0.25 $A \cdot g^{-1}$, which was ~53 $F \cdot g^{-1}$ higher than that of the MnO_2–CFP electrode. Furthermore, it could retain over half of its photo-induced capacity enhancement (~56%) even after the visible light irradiation was shut off for 12 h, which could be attributed to its slow release of stored charges from its specific electronic band structure to assure its long-lasting capacity enhancement in dark after the visible light charging was over.

2 Materials and methods

2. 1 Chemicals and materials

Potassium permanganate ($KMnO_4$), concentrated nitric acid (HNO_3, 36%), and acetone were purchased from Sinopharm Chemical Reagent Co., Ltd. (Shanghai, China). Cerium nitrate ($Ce(NO_3)_3 \cdot 6H_2O$, 99.99%) was purchased from Adamas Reagent., Ltd. (Shanghai, China). Sodium sulfate (Na_2SO_4) was purchased from Aladdin Industrial Corporation Co., Ltd. (Shanghai, China). CFP (TGP-H-060, thickness = 0.19 mm) was purchased from Toray Industries (China) Co., Ltd. (Shanghai, China). All the chemicals were analytical grade and used without further purification. High-purity deionized water with a resistivity of 18.25 MΩ·cm prepared from an ultra-pure water purifier (PCDX-B, Chengdu Pure Technology Co., Ltd., China) was used throughout the experimental process.

2. 2 Synthesis of the MnO_2–CFP sample

MnO_2–CFP composites were prepared via a robust

hydrothermal process with modifications [43–45]. Prior to the synthesis, CFP (2 cm × 3 cm) was pretreated successively with acetone, 10% hydrochloric acid, deionized water, and ethanol under ultrasonic cleaning, and finally dried in an oven overnight at 60 ℃. In a typical synthesis, 0.75 mM $KMnO_4$ was dissolved in deionized water (35 mL) under constant magnetic stirring for 30 min, and then transferred into a Teflon-lined stainless-steel autoclave. In the meantime, CFP was placed into the $KMnO_4$ solution, and a hydrothermal reaction was undertaken at 150 ℃ for 6 h. After cooling down to room temperature naturally, CFP coated with a brown-black product was taken out from the autoclave, washed several times with deionized water and ethanol, and then dried at 60 ℃ in air for 12 h to obtain the MnO_2–CFP sample. For comparison purpose, MnO_2 nanoparticles were also synthesized with the same hydrothermal process except for the placing of CFP into the $KMnO_4$ solution.

2. 3 Synthesis of the CeO_2/MnO_2–CFP sample

0.024 g $Ce(NO_3)_3·6H_2O$ was dissolved in 30 mL deionized water with moderate stirring magnetically for 30 min. Then, the as-obtained solution and a piece of the as-prepared MnO_2–CFP substrate were transferred into a Teflon-lined stainless-steel autoclave and heated at 90 ℃ for 6 h in an oven to deposit CeO_2 nanoparticles onto MnO_2 through the redox reaction between Ce^{3+} and MnO_2 [46]. After cooling down to room temperature naturally, it was taken out from the autoclave, washed several times with deionized water and ethanol, and then dried at 60 ℃ in air for 12 h to obtain the CeO_2/MnO_2–CFP sample. For comparison purpose, CeO_2 nanoparticles were also synthesized by a water bath method, in which 0.6 g $Ce(NO_3)_3·6H_2O$ was firstly added into 200 mL of deionized water and stirred for 10 min. Then, 5 g hexamethylenetetramine ($C_6H_{12}N_4$) was added into the solution under magnetic stirring for another 10 min. Finally, the solution was placed in a water bath at 90 ℃ for 1 h under continuous stirring to obtain CeO_2 nanoparticles.

2. 4 Material characterization

The crystal structures of the as-prepared samples were investigated by the X-ray diffractometer (Empyrean, Malvern Panalytical, the Netherlands). Their morphologies were observed by both the field emission scanning electron microscope (FESEM; JSM-7610F, JEOL, Japan) and the transmission electron microscope (TEM; JEM-2100F, JEOL, Japan) equipped with a mapping system. The X-ray photoelectron spectroscopy (XPS) was obtained on an X-ray photoelectron spectrometer (ESCALAB 250Xi, Thermo Scientific, USA) with a monochromatized Al Kα X-ray source, and a spectrophotometer (UV-3600Plus, Shimadzu Corporation, Japan) was used to measure the optical absorbance spectra of these samples. The element ratios were confirmed by the inductively coupled plasma optical emission spectrometer (5110 ICP-OES, Agilent, USA).

2. 5 Electrochemical measurements

The electrochemical performances of the as-prepared samples were measured by an electrochemical workstation (CHI760E, Shanghai Chenhua Instrument Co., Ltd., China) in a 1 M Na_2SO_4 electrolyte at room temperature with a three-electrode system. CFP, MnO_2–CFP, and CeO_2/MnO_2–CFP samples of 1 cm × 1 cm in area were directly used as working electrodes. The CeO_2 working electrode was prepared by a slurry coating procedure. CeO_2 nanoparticles, acetylene black, and polyvinylidene fluoride (PVDF) were first mixed uniformly in a weight ratio of 8 : 1 : 1, and then dispersed in N-methylpyrrolidone (NMP) to form a uniform slurry. The slurry was coated on a CFP sample of 1 cm × 1 cm in area, and then dried at 60 ℃ for 12 h. A platinum plate was used as the counter electrode, and an Ag/AgCl electrode was used as the reference electrode. The mass loadings of active materials on CFP were all controlled at ~1.4 $mg·cm^{-2}$. The light source was a 300 W xenon lamp (PLS-SXE300+, Beijing Perfect Light Technology Co., Ltd., China) with filters to provide visible light illumination (400–780 nm) or visible/infrared illumination (400–2200 nm). A circulation cooling water system was used to keep the temperature stable during the performance measurement.

3 Results and discussion

3. 1 Creation of the CeO_2/MnO_2–CFP sample

The CeO_2/MnO_2–CFP sample was prepared by a facile, two-step *in-situ* growth method with CFP as the substrate. Figure 1(a) compares the X-ray diffraction (XRD) patterns of MnO_2–CFP and CeO_2/MnO_2–CFP samples. Both samples demonstrated the typical peaks of CFP at 2θ of ~26.4° and 54.5° from their CFP

substrates, while a tiny peak at 2θ of ~12.5° could be observed in the XRD patterns of both samples, which could be ascribed to the (002) peak of MnO_2 (JCPDS: 18-0802). Thus, the XRD analysis results confirmed the successful formation of MnO_2 on the CFP surface. The inset in Fig. 1(a) shows their magnified XRD patterns from 2θ of ~28° to 80°, which demonstrated that several new diffraction peaks at 2θ of ~28.54°, 33.07°, 47.47°, and 56.33° emerged for the CeO_2/MnO_2–CFP sample, corresponding to (111), (200), (220), and (331) peaks of the cubic CeO_2 phase (JCPDS: 81-0792), respectively. Thus, the CeO_2/MnO_2–CFP sample was successfully created by the second *in-situ* growth step of our approach through the decoration of CeO_2 nanoparticles on the MnO_2–CFP sample.

Figure S1(a) in the Electronic Supplementary Material (ESM) shows the SEM image of the MnO_2–CFP sample, which demonstrated that a dense MnO_2 layer was uniformly coated on the surface of carbon fibers, resulting in a three-dimensional interweaved structure. This structure was highly porous with a large surface area, which was beneficial for the efficient transportation and diffusion of electrons and electrolyte ions. Figure 1(b) shows the SEM image of the CeO_2/MnO_2–CFP sample, which clearly demonstrated that the deposition of CeO_2 nanoparticles on the MnO_2–CFP sample did not change its whole three-dimensional interweaved structure. The inset in Fig. 1(b) shows the magnified image of the dense layer on carbon fibers of the CeO_2/MnO_2–CFP sample, which demonstrated that brighter CeO_2 nanoparticle clusters were deposited on the MnO_2 layer. This observation was consistent with the CeO_2 deposition process, in which a redox reaction between Ce^{3+} ions and MnO_2 happened to oxidize Ce^{3+} to Ce^{4+} for the creation of CeO_2 nanoparticles [46].

Figure 1(c) shows the energy dispersive spectroscopy (EDS) mapping results of detached particles from the CeO_2/MnO_2–CFP sample through ultra-sonification. The top left image demonstrates that they were agglomerates of irregular nanoparticles with the size from a few to tens of nanometers. The other three parts in Fig. 1(c) show the signals of Mn, Ce, and O elements within the square area in the top left image, which demonstrated

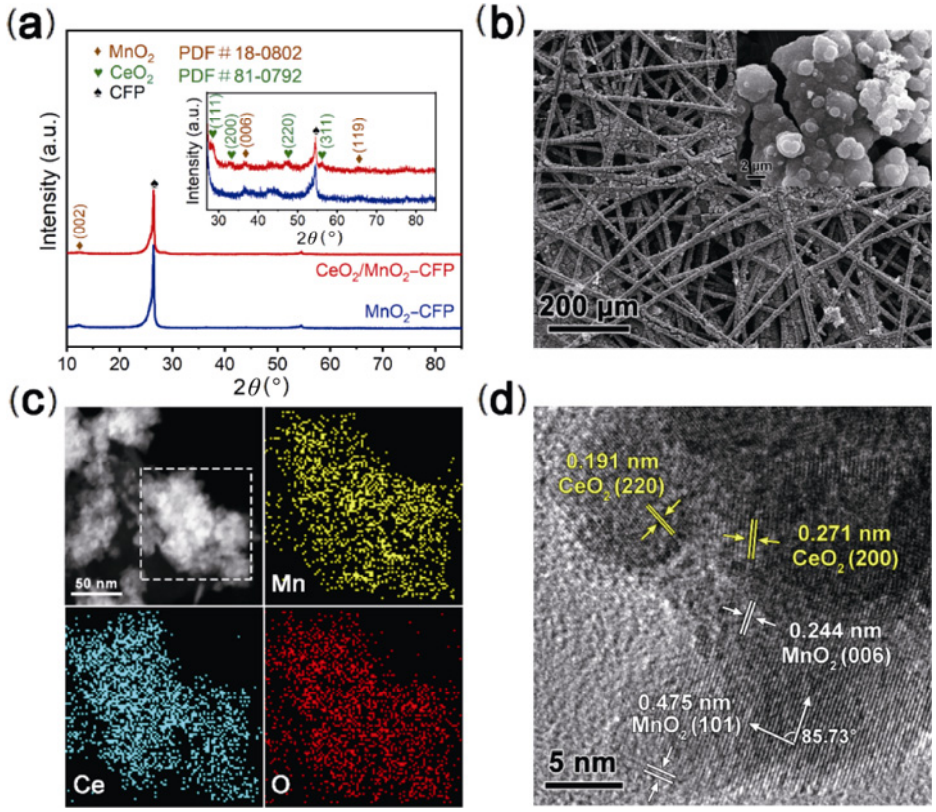

Fig. 1 (a) XRD patterns of MnO_2–CFP and CeO_2/MnO_2–CFP samples. The inset shows their magnified XRD patterns from 2θ of ~28° to 80°. (b) SEM image of the CeO_2/MnO_2–CFP sample. The inset shows the magnified image of the dense layer. (c) EDS mapping results of detached particles from the CeO_2/MnO_2–CFP sample. (d) HRTEM image of the CeO_2/MnO_2–CFP sample.

that Mn, Ce, and O elements were uniformly distributed in the CeO_2/MnO_2 composite. The composition ratio between CeO_2 and MnO_2 was evaluated further by the ICP-OES, and the result was shown in Table S1 in the ESM. The atomic ratio between Mn and Ce could be calculated at ~7.78 : 1.

Figure 1(d) shows the representative high-resolution TEM (HRTEM) image of the CeO_2/MnO_2–CFP sample. In the lower part of the image, two sets of lattice planes with *d*-spacing values of ~0.244 and ~0.475 nm could be clearly observed with the interfacial angle of ~85.73°, which matched well with the (006) and (101) planes of the MnO_2 phase, respectively. In the upper part of the image, parallel lattice planes with *d*-spacing values of ~0.191 and ~0.271 nm could be clearly observed, which could be assigned to the (220) and (200) planes of the cubic CeO_2 phase, respectively. The HRTEM observation demonstrated that nanosized CeO_2 crystals were decorated on MnO_2 crystals with good contacts between them, which was consistent with the CeO_2 deposition process through the redox reaction between Ce^{3+} and MnO_2 and beneficial for charge carriers to transfer between them [46].

3. 2 Chemical composition of the CeO_2/MnO_2–CFP sample

The XPS was further used to investigate the surface chemical compositions and element valence states of obtained samples. Figure 2(a) shows the XPS survey spectrum of the CeO_2/MnO_2–CFP sample, and that of the MnO_2–CFP sample could be found in Fig. S1(b) in the ESM. Both samples had XPS signals of C, Mn, and O elements, while additional XPS peaks belonged to Ce element could be clearly observed on the survey spectrum of the CeO_2/MnO_2–CFP sample as expected. Thus, it further demonstrated clearly that CeO_2 nanoparticles were successfully decorated on the MnO_2–CFP sample surface in the second-step *in-situ* growth of our approach.

Figure 2(b) shows the high-resolution XPS spectra of Mn 2p peaks of the CeO_2/MnO_2–CFP sample, and that of the MnO_2–CFP sample could be found in Fig. S1(c) in the ESM. Both of their Mn 2p peaks could be best fitted by the combination of four peaks. For the CeO_2/MnO_2–CFP sample, the two fitted peaks at ~654.7 and ~643.3 eV belonged to Mn^{4+} $2p_{1/2}$ and

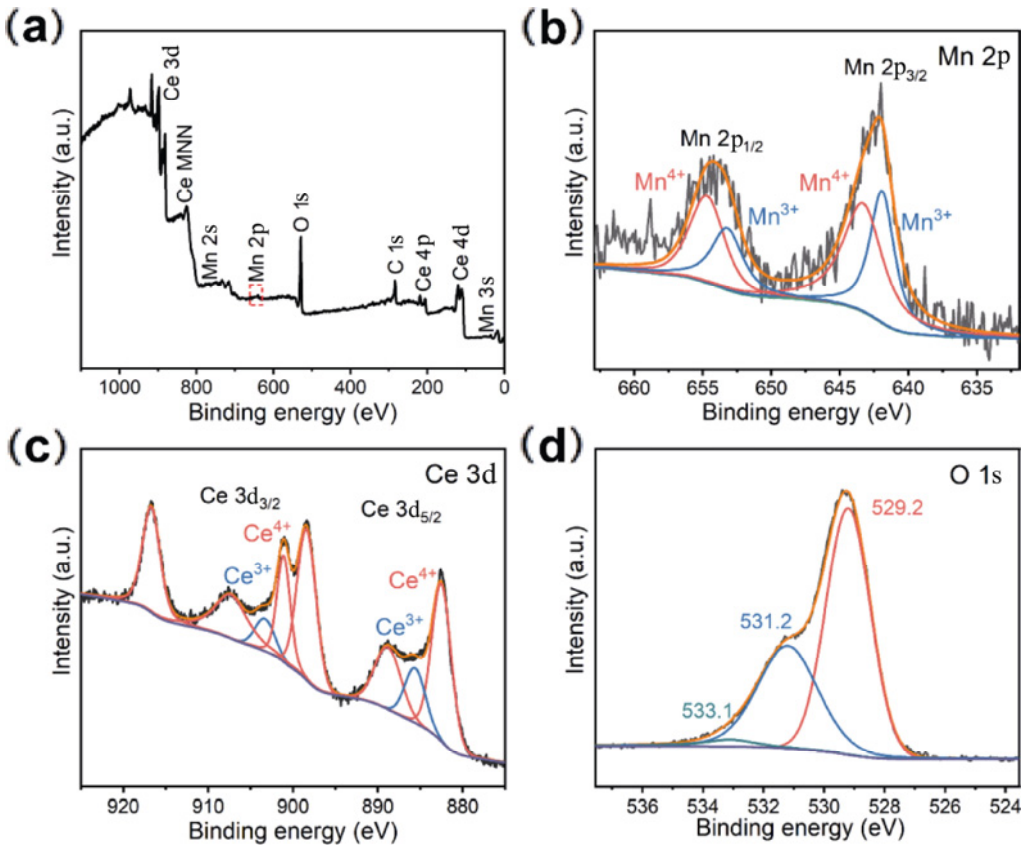

Fig. 2 (a) XPS survey spectrum and (b, c, d) high-resolution XPS scans over Mn 2p, Ce 3d, and O 1s peaks of the CeO_2/MnO_2–CFP sample, respectively.

Mn^{4+} $2p_{3/2}$, respectively; and the other two fitted peaks at ~653.2 and ~641.9 eV could be assigned for Mn^{3+} $2p_{1/2}$ and Mn^{3+} $2p_{3/2}$, respectively. For the MnO_2–CFP sample, the two fitted peaks at ~654.1 and ~642.6 eV belonged to Mn^{4+} $2p_{1/2}$ and Mn^{4+} $2p_{3/2}$, respectively; and the other two fitted peaks at ~653.2 and ~641.9 eV could be assigned for Mn^{3+} $2p_{1/2}$ and Mn^{3+} $2p_{3/2}$, respectively [47–50]. It could be found that the ratio of Mn^{4+}/Mn^{3+} decreased from 2.46 for the MnO_2–CFP sample to 1.38 for the CeO_2/MnO_2–CFP sample after the decoration of CeO_2 nanoparticles. This observation was consistent with the fact that CeO_2 nanoparticles were grown on the MnO_2 surface through the redox reaction [46], which could form a good contact interface between them to benefit the electron transfer between them.

Figure 2(c) shows the high-resolution XPS spectra of Ce 3d peaks of the CeO_2/MnO_2–CFP sample. The three peaks centered at ~882.5, ~888.8, and ~898.4 eV could be assigned to Ce^{4+} $3d_{5/2}$, the three peaks centered at ~901.1, ~907.3, and ~916.7 eV could be assigned to Ce^{4+} $3d_{3/2}$, and another two peaks located at ~885.6 and ~903.3 eV corresponded to Ce^{3+} $3d_{5/2}$ and Ce^{3+} $3d_{3/2}$, respectively [51–53]. The Ce^{3+}/Ce^{4+} ratio was determined at 0.13, and the coexistence of Ce^{4+} and Ce^{3+} could be attributed to the use of $Ce(NO_3)_3{\cdot}6H_2O$ as the Ce source during the synthesis process.

Figure 2(d) shows the high-resolution XPS spectra of O 1s peaks of the CeO_2/MnO_2–CFP sample, and that of the MnO_2–CFP sample could be found in Fig. S1(d) in the ESM. Both of their O 1s peaks could be best fitted by the combination of three peaks, including lattice oxygen (metal–oxygen bonds at ~529.2 eV for the CeO_2/MnO_2–CFP sample and at ~529.7 eV for the MnO_2–CFP sample), surface adsorbed oxygen (at ~531.2 eV for both samples), and adsorbed H_2O (at ~533.1 eV for both samples) [51,53,54].

3. 3 Band structure and photo-generated charge carrier separation behaviors of the CeO_2/MnO_2–CFP sample

The diffuse reflectance spectrum measurement was used to reveal the optical properties of the obtained samples. Figures 3(a) and 3(b) show the light absorbance curves of MnO_2 and CeO_2 nanoparticles, respectively, which were approximated by the Kubelka–Munk function from their diffuse reflectance data [55,56]. As expected, MnO_2 nanoparticles demonstrated a wide range of light absorption from the ultraviolet (UV) range into the near-infrared region [57]. The inset in Fig. 3(a) shows the Tauc plots ($(F(R)h\nu)^2$ vs. $h\nu$) of MnO_2 nanoparticles (direct band gap semiconductor) constructed from their light absorbance data [58,59], from which its band gap value could be determined at ~1.57 eV. For CeO_2 nanoparticles, they demonstrated a light absorption from the UV range just into the visible light region [60]. The inset in Fig. 3(b) shows the Tauc plots ($(F(R)h\nu)^{1/2}$ vs. $h\nu$) of CeO_2 nanoparticles (indirect band gap semiconductor) constructed from their light absorbance data [61], from which its band gap value could be determined at ~3.06 eV.

Figures 3(c) and 3(d) show the Mott–Schottky (M–S) plots of MnO_2 and CeO_2 nanoparticles measured at 1 kHz and vs. Ag/AgCl reference electrode at pH = 7, respectively. Both of their M–S plots showed positive slopes, which indicated that they were both n-type semiconductors. Based on the intercepts of their M–S plots, their flat band potentials vs. the Ag/AgCl electrode could be calculated at ~1.20 V for MnO_2 nanoparticles and ~−0.51 V for CeO_2 nanoparticles. The electrode potential of Ag/AgCl is 0.2224 V vs. normal hydrogen electrode (NHE) at pH = 7. Thus, their flat band potentials vs. NHE could be calculated at ~1.42 V for MnO_2 nanoparticles and ~−0.29 V for CeO_2 nanoparticles. For n-type semiconductors, their flat band potentials are generally ~0.2 V more positive than their conduction band minimums (CBMs) [62]. So, the CBM of MnO_2 nanoparticles could be determined at ~1.22 V, and the CBM of CeO_2 nanoparticles could be determined at ~−0.49 V. Combined with their band gap values, the valence band maximums (VBMs) of MnO_2 and CeO_2 samples could be determined at ~2.79 and ~2.57 V, respectively.

Figure 3(e) shows the band structure of the CeO_2/MnO_2 heterojunction from the above analysis results, which demonstrated that it had a type II semiconductor heterojunction. Their aligned band structure could facilitate the separation of photo-generated charge carriers, which could minimize the well-known photo-generated charge carrier recombination problem in MnO_2 [63–65]. Thus, more photo-generated charge carriers could participate in the photo-assisted charging process, which should ensure the desired photo-assisted charging capability to supercapacitors with MnO_2-based active materials.

Figure 3(f) compares the photocurrent measurement results of the MnO_2–CFP and CeO_2/MnO_2–CFP samples

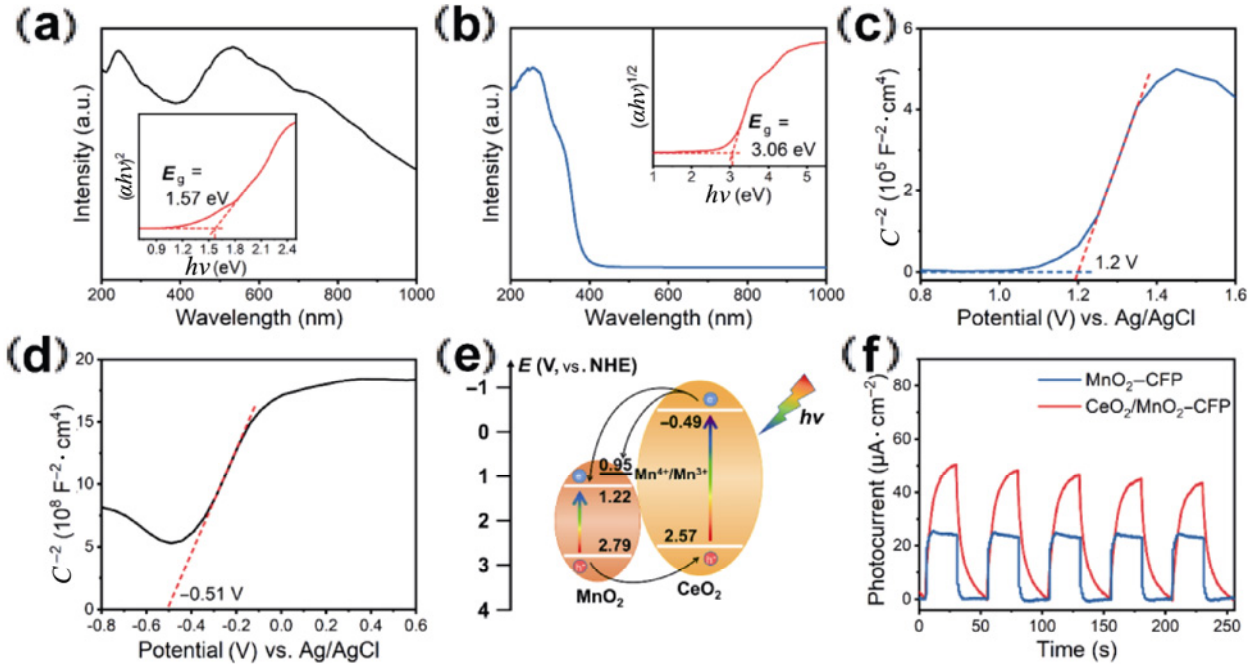

Fig. 3 (a, b) Light absorbance curves of MnO_2 and CeO_2 nanoparticles, respectively. The insets show their Tauc plots constructed from their light absorbance data. (c, d) M–S plots of MnO_2 and CeO_2 nanoparticles measured at 1 kHz and vs. Ag/AgCl reference electrode, respectively. (e) Band structure diagram of the CeO_2/MnO_2 heterojunction. (f) Photocurrent measurement results of the MnO_2–CFP and CeO_2/MnO_2–CFP samples under visible light illumination at an applied voltage of 0.6 V.

under visible light illumination. The photocurrent densities of the CeO_2/MnO_2–CFP sample were obviously higher than those of the MnO_2–CFP sample, which was consistent with the theoretical prediction that the CeO_2/MnO_2 heterojunction could facilitate the photo-generated charge carrier separation and transfer as expected from their matching band structure, as shown in Fig. 3(e). Furthermore, another clear difference existed between their photocurrent behaviors. The photocurrent of the CeO_2/MnO_2–CFP sample showed a gradual decrease behavior when the light illumination was shut off, while that of the MnO_2–CFP sample decreased sharply to zero when the light illumination was just shut off. This observation indicated that part of the photo-generated electrons could be effectively retained by the CeO_2/MnO_2–CFP sample under visible light illumination, and then slowly released to generate the current in dark when the illumination was shut off, which was consistent with their band structure analysis result.

3. 4 Photo-assisted charging of the CeO_2/MnO_2–CFP sample

The electrochemical performances of pure CFP, the MnO_2–CFP sample, and the CeO_2/MnO_2–CFP sample electrodes were evaluated in the traditional three-electrode system. Figure 4(a) compares the cyclic voltammetry (CV) curves of pure CFP, the MnO_2–CFP, and the CeO_2/MnO_2–CFP electrodes in dark at the scan rate of 5 $mV\cdot s^{-1}$, which clearly demonstrated that both CFP and CeO_2 electrodes had very little capacitance. Thus, they could not contribute much to the capacitances of the MnO_2–CFP and the CeO_2/MnO_2–CFP electrodes. The capacitances of the MnO_2–CFP and the CeO_2/MnO_2–CFP electrodes were quite close in dark because their main capacitance contributions came from the same pseudocapacitive active material of MnO_2. Due to the very low capacitance of CeO_2, the amount of CeO_2 in the CeO_2/MnO_2–CFP electrode should be small in our CeO_2/MnO_2–CFP sample (atomic ratio between Mn and Ce at ~7.78:1). Otherwise, a high amount of CeO_2 will lower the intrinsic capacitance of CeO_2/MnO_2–CFP sample.

Figures 4(b) and 4(c) show the CV curves of the MnO_2–CFP and the CeO_2/MnO_2–CFP electrodes in dark and under visible light illumination (400–780 nm) at the scan rate of 5 $mV\cdot s^{-1}$, respectively. It demonstrated that the capacitances of both electrodes under visible light illumination were higher than those in dark, while the photo-induced capacitance increase of the $CeO_2/$

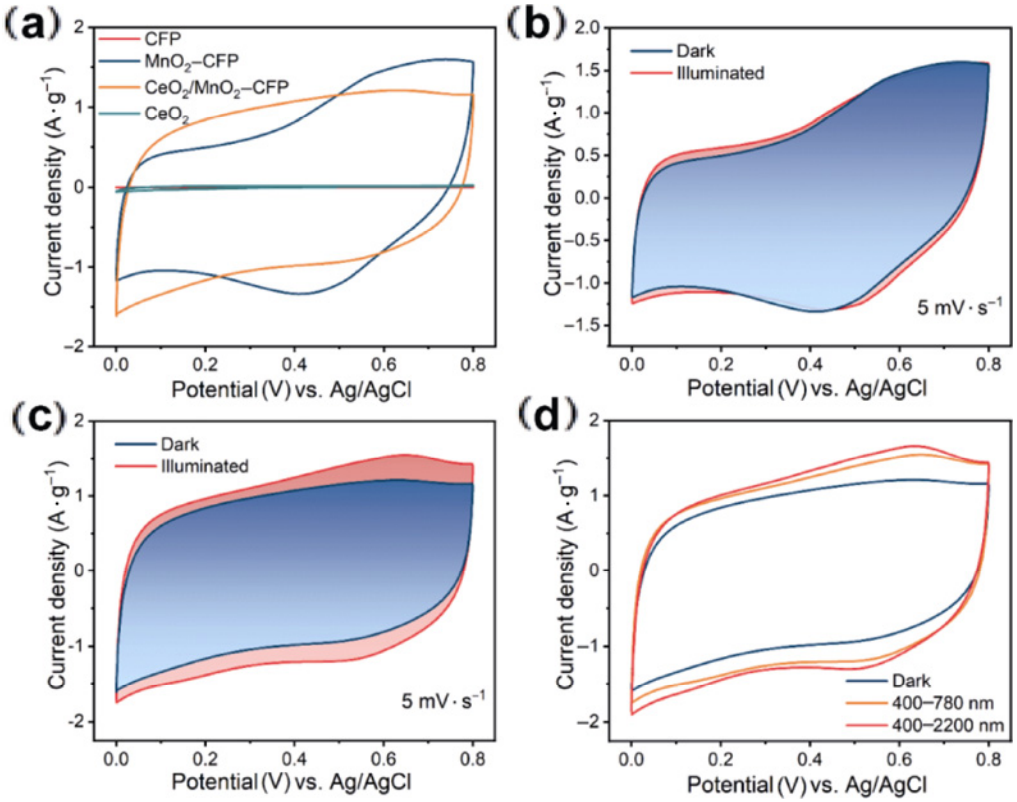

Fig. 4 (a) CV curves of pure CFP, pure CeO_2, MnO_2–CFP, and CeO_2/MnO_2–CFP electrodes in dark at the scan rate of 5 $mV·s^{-1}$. (b, c) CV curves of MnO_2–CFP and CeO_2/MnO_2–CFP electrodes in dark and under visible light illumination (400–780 nm) at the scan rate of 5 $mV·s^{-1}$, respectively. (d) CV curves of the CeO_2/MnO_2–CFP electrode in dark, under visible light illumination, and under visible/infrared illumination (400–2200 nm) at the scan rate of 5 $mV·s^{-1}$.

MnO_2–CFP electrode was much higher than that of the MnO_2–CFP electrode. From their CV curves, the overall specific capacitance of the MnO_2–CFP electrode at the scan rate of 5 $mV·s^{-1}$ was calculated at ~182 $F·g^{-1}$ in dark and ~190 $F·g^{-1}$ under visible light illumination, representing an increase of only ~4%. For the CeO_2/MnO_2–CFP electrode, however, its overall specific capacitance at the scan rate of 5 $mV·s^{-1}$ increased from ~187 $F·g^{-1}$ in dark largely to ~229 $F·g^{-1}$ under visible light illumination, representing an significant increase of ~22%. Figure S2 in the ESM further shows their CV curves in dark and under visible light illumination at scan rates of 10 and 20 $mV·s^{-1}$. Their specific capacitance and increase percentage data were summarized in Table S2 in the ESM. It was clear that the photo-induced capacitance increase in the CeO_2/MnO_2–CFP electrode was from ~22% to ~27% when the scan rates were from 5 to 20 $mV·s^{-1}$, while that of the MnO_2–CFP electrode was only from ~4% to 10%.

Figure 4(d) shows the CV curves of the CeO_2/MnO_2–CFP electrodes in dark, under visible light illumination, and under visible/infrared illumination (400–2200 nm) at the scan rate of 5 $mV·s^{-1}$. It demonstrated clearly that the photo-induced capacitance enhancement of the CeO_2/MnO_2–CFP electrode could be affected by the light source. Under visible/infrared illumination, its overall specific capacitance at the scan rate of 5 $mV·s^{-1}$ could be calculated at ~240 $F·g^{-1}$, which represented an increase of 28% compared with that in dark and a further increase of 5% compared with that under visible light illumination. Due to its narrow gap semiconductor nature (E_g = ~1.57 eV), part of the infrared illumination could generate electron–hole pairs in MnO_2 for the photo-assisted charging to enhance its capacitance. Thus, the CeO_2/MnO_2–CFP electrode could effectively use the abundant solar energy input to provide a green and economic way to enhance its capacitance.

3.5 Galvanostatic charging and discharging (GCD) behaviors of the CeO_2/MnO_2–CFP electrode

The photo-induced capacitance enhancement of the CeO_2/MnO_2–CFP electrode was further confirmed by

the GCD profiles. Figures 5(a) and 5(b) show the GCD profiles of the MnO_2–CFP and the CeO_2/MnO_2–CFP electrodes in dark and under visible light illumination at a charging and discharging current density of 0.25 $A \cdot g^{-1}$, respectively. For the MnO_2–CFP electrode, its capacitance increased just from ~240 $F \cdot g^{-1}$ in dark to ~250 $F \cdot g^{-1}$ under visible light illumination, representing an increase of only ~4%. For the CeO_2/MnO_2–CFP electrode, however, its capacitance increased from ~254 $F \cdot g^{-1}$ in dark to ~303 $F \cdot g^{-1}$ under visible light illumination, representing an increase of ~19%. Figures S3(a) and S3(b) in the ESM show the GCD profiles of the MnO_2–CFP electrode in dark and under visible light illumination at a series of charging and discharging current densities between 0.25 and 2.5 $A \cdot g^{-1}$, respectively, and those of the CeO_2/MnO_2–CFP electrode are shown in Figs. S3(c) and S3(d) in the ESM, respectively. From these data, their corresponding specific capacitances and photo-induced capacitance increase percentages at a series of charging and discharging current densities were calculated and shown in Figs. 5(c) and 5(d) for the MnO_2–CFP and the CeO_2/MnO_2–CFP electrodes, respectively. It could also be found that the capacitances of both electrodes under visible light illumination were higher than those in dark, while the photo-induced capacitance increase of the CeO_2/MnO_2–CFP electrode was much higher than that of the MnO_2–CFP electrode. For the CeO_2/MnO_2–CFP electrode, the photo-assisted charging increased its specific capacitance relatively steadily for ~41–49 $F \cdot g^{-1}$ when the charging and discharging current densities were from 0.25 to 2.5 $A \cdot g^{-1}$, while that of the MnO_2–CFP electrode under the same charging and discharging current density range was only ~10–20 $F \cdot g^{-1}$. These results were consistent with the CV curve measurement results, which further confirmed that the decoration of a small amount of CeO_2 nanoparticles on the MnO_2–CFP electrode largely improved its photo-assisted charging capability.

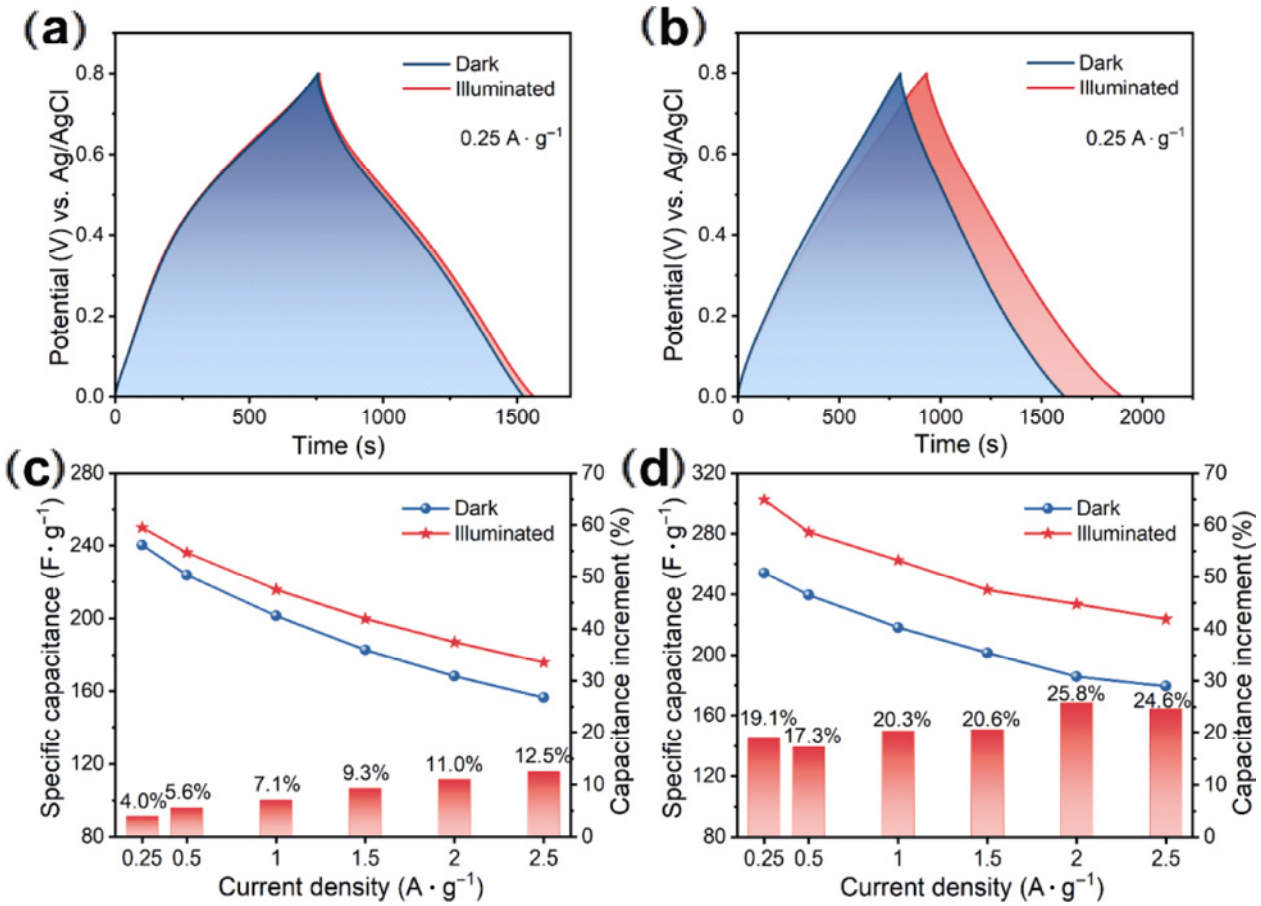

Fig. 5 GCD profiles of (a) MnO_2–CFP and (b) CeO_2/MnO_2–CFP electrodes in dark and under visible light illumination at a charging and discharging current density of 0.25 $A \cdot g^{-1}$. Specific capacitances and photo-induced capacitance increase percentages of (c) MnO_2–CFP and (d) CeO_2/MnO_2–CFP electrodes at a series of charging and discharging current densities in dark and under visible light illumination.

3. 6 Stability and retainment of photo-assisted charging effect in dark of the CeO_2/MnO_2–CFP electrode

The capacitance stability is critical for the potential application of a supercapacitor. Figure 6(a) shows the cycling performances of the CeO_2/MnO_2–CFP electrode in dark and under visible light illumination at the charging and discharging current density of 1 $A \cdot g^{-1}$. The result demonstrated that its intrinsic capacitance in dark and photo-induced capacitance enhancement were both quite stable during the cycling usage. After 100 cycles, no deterioration was observed for both its intrinsic capacitance in dark and its photo-induced capacitance enhancement. This observation indicated that the CeO_2/MnO_2–CFP electrode had a strong structure, and the interfaces of CeO_2/MnO_2 and MnO_2/CFP were robust. Actually, its specific capacitance showed a slight increase at the beginning of the cycling experiment, which may be attributed to its required electrochemical activation during the initial stage [66,67].

More interestingly, the CeO_2/MnO_2–CFP electrode demonstrated a retainment capability of photo-induced capacitance enhancement in dark for an extended period of time after the illumination was switched off. Figure 6(b) shows the CV curves of the CeO_2/MnO_2–CFP electrode at the scan rate of 5 $mV \cdot s^{-1}$ in dark, under visible light illumination, and in dark after the illumination was switched off for 12 h. It demonstrated clearly that the CeO_2/MnO_2–CFP electrode could keep part of its photo-induced capacitance enhancement in dark for a quite long period of time. Even after the illumination was switched off for 12 h, its specific capacitance was still ~222 $F \cdot g^{-1}$, which was still ~22 $F \cdot g^{-1}$ higher than that in dark and represented a retainment of its photo-induced capacitance enhancement of ~56%. For comparison, the CV curves of the MnO_2–CFP electrode at the scan rate of 5 $mV \cdot s^{-1}$ in dark, under visible light illumination, and in dark after the illumination was switched off for only 0.5 h were shown in Fig. S4 in the ESM. After the illumination was switched off for only 0.5 h, its CV curve already changed back to overlap with its CV curve in dark, which suggested that the MnO_2–CFP electrode could not retain part of its photo-induced capacitance enhancement after the illumination was switched off. Thus, the comparison results clearly demonstrated that the decoration of a small amount of CeO_2 nanoparticles on the MnO_2–CFP electrode could also endow the CeO_2/MnO_2–CFP electrode a long-lasting capability to retain a large part of its photo-induced capacitance enhancement in dark.

3. 7 Photo-assisted charging mechanism of the CeO_2/MnO_2–CFP sample

It is well known that the electrochemical energy storage is dominated by two mechanisms: One is the surface capacitive process, and the other is the surface redox reaction and/or insertion/intercalation-based process [68]. According to the theory by Ardizzone *et al*. [69] and Baronetto *et al*. [70], the charge Q has two components, as described in Eq. (1):

$$Q_{total} = Q_{surface} + Q_{pseudo} \quad (1)$$

where Q_{total} is the total charge that can be stored, $Q_{surface}$ is the surface contribution that mainly stems from physical adsorption, and Q_{pseudo} is the pseudocapacitive contribution. Figure 7(a) shows the

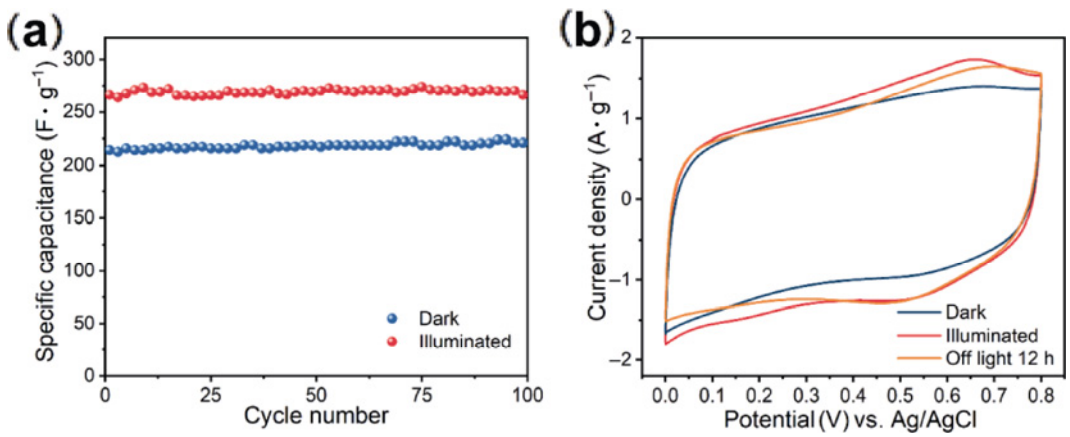

Fig. 6 (a) Cycling performances of the CeO_2/MnO_2–CFP electrode in dark and under visible light illumination at the charging and discharging current density of 1 $A \cdot g^{-1}$. (b) CV curves of the CeO_2/MnO_2–CFP electrode at the scan rate of 5 $mV \cdot s^{-1}$ in dark, under visible light illumination, and in dark after the illumination was switched off for 12 h.

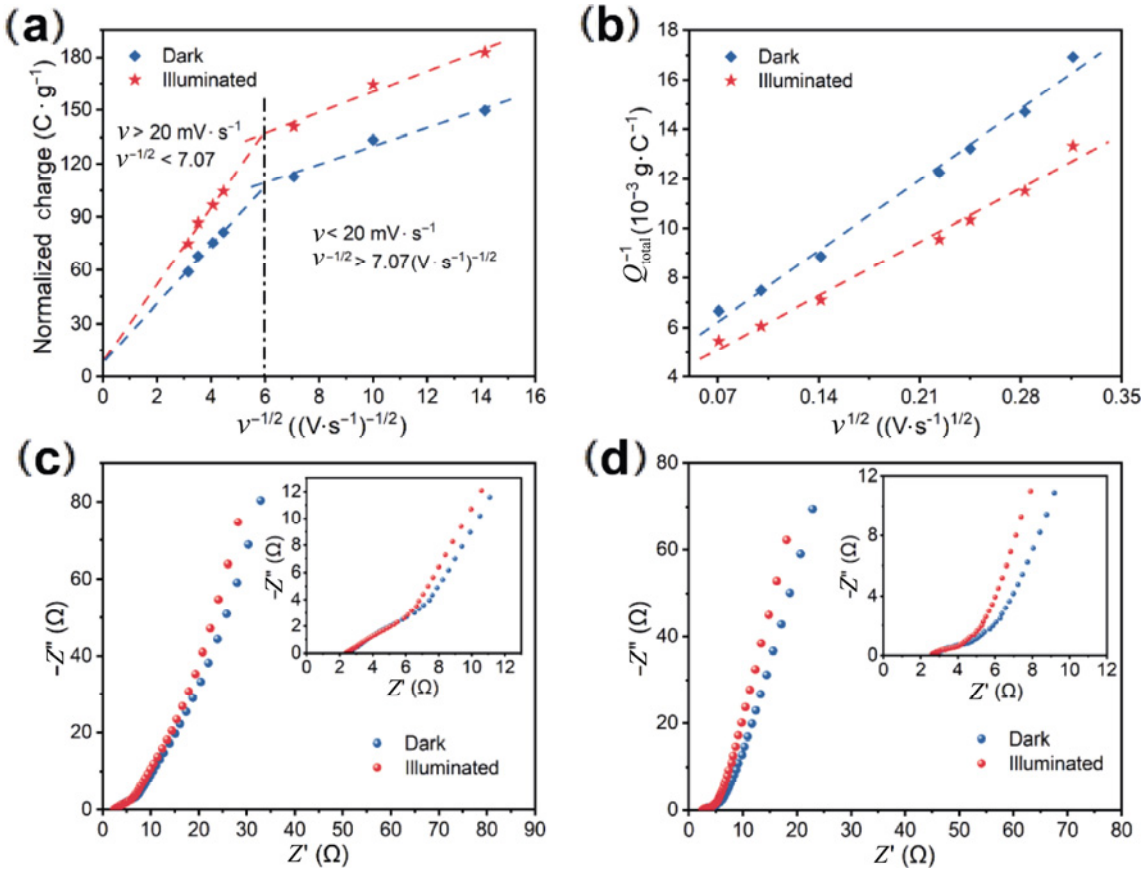

Fig. 7 (a, b) Plots of Q_{total} vs. $v^{-1/2}$ and Q_{total}^{-1} vs. $v^{1/2}$ of the CeO_2/MnO_2–CFP electrode in dark and under visible light illumination, respectively. (c, d) Nyquist plots of MnO_2–CFP and CeO_2/MnO_2–CFP electrodes in dark and under visible light illumination at open circuit potential, respectively.

plots of Q_{total} vs. $v^{-1/2}$ of the CeO_2/MnO_2–CFP electrode in dark and under visible light illumination, in which two distinct regions existed with the scan rate of 20 mV·s^{-1} (7.07 (V·s^{-1})$^{-1/2}$) as the boundary. When the scan rate was over 20 mV·s^{-1} ($v^{-1/2}$ was lower than 7.07 (V·s^{-1})$^{-1/2}$), the Q_{total} value decreased linearly with the scan rate increase, indicating a diffusion-controlled energy storage process. Therefore, the intersection of the extrapolated plot with the *y*-axis of this region could reveal the charge associated with the most accessible area ($Q_{surface}$) [71]. Figure 7(a) demonstrates that the capacitance ($Q_{surface}$) values of the CeO_2/MnO_2–CFP electrode from the most accessible area in dark and under illumination were almost identical at ~7.83 and ~7.47 C·g^{-1}, respectively, which indicated that visible light illumination had no obvious impact on the adsorption of protons onto the interface between the CeO_2/MnO_2–CFP electrode and the electrolyte.

Figure 7(b) shows the plots of Q_{total}^{-1} vs. $v^{1/2}$ of the CeO_2/MnO_2–CFP electrode in dark and under visible light illumination. When the scan rate was infinitesimal, both the surface contribution and the pseudocapacitive contribution fully co-existed. Thus, the intersection of the extrapolated plot with the *y*-axis in Fig. 7(b) could reveal its Q_{total}, and it was found that the Q_{total} values of the CeO_2/MnO_2–CFP electrode were ~294.12 and ~344.83 C·g^{-1} in dark and under visible light illumination, respectively. So, Q_{pseudo} values of the CeO_2/MnO_2–CFP electrode were ~286.29 and ~337.36 C·g^{-1} in dark and under visible light illumination, respectively. Thus, the pseudocapacitive contribution dominated in the electrochemical energy storage of the CeO_2/MnO_2–CFP electrode, and its observed large photo-assisted charging effect came mostly from its Q_{pseudo} enhancement under visble light illumination due to the participation of abundant photo-generated charge carriers in the oxidation/reduction reactions to enhance its energy storage.

The electrochemical impedance spectroscopy experiments were carried out on both the MnO_2–CFP and the CeO_2/MnO_2–CFP electrodes in dark and under visible light illumination in a frequency range between

0.01 Hz and 100 kHz. Figures 7(c) and 7(d) show their Nyquist plots in dark and under visible light illumination at open circuit potential. For both of them, two distinct parts could be found in their Nyquist plots, including an imperfect half semicircle in the middle- to high-frequency regions, and a sloped straight line in the low-frequency region. The straight line in the low-frequency region had a finite slope, which could represent the diffusive behaviors of the electrolyte in the electrode pores and ions in active materials. For both of them, their slopes of straight lines in the low-frequency region under visible light illumination were higher than those in dark, which suggested that visible light illumination could enhance their electric conductivities due to photo-generated charge carriers. The imperfect half semicircle in the middle- to high-frequency range could be associated with the surface properties of the electrode and corresponded to the charge-transfer resistance (R_{ct}).

Figure S5 in the ESM shows the illustration of the equivalent circuit with a set of resistors and constant phase elements (CPE, denoted as Q) in series and parallel, where R_s is the series resistance, Q_{dl} and Q_{ps} are the double-layer capacitance and pseudo-capacitance, respectively, and W is the Warburg diffusion. Table S3 in the ESM summarizes their parameters of different elements in their equivalent circuits. For both of them, their R_{ct} decreased under visible light illumination, which suggested that they had an easier charge transfer in them with illumination [72]. The R_{ct} of the CeO_2/MnO_2–CFP electrode decreased from ~2.77 Ω in dark to ~1.62 Ω under visible light illumination, while that of the MnO_2–CFP electrode decreased from ~8.50 Ω only to ~5.40 Ω. This observation demonstrated that the charge transfer resistance in the CeO_2/MnO_2–CFP electrode was much lower than that in the MnO_2–CFP electrode, which further verified that the decoration of a small amount of CeO_2 nanoparticles on the MnO_2–CFP sample surface did facilitate the photogenerated charge carrier separation and transfer.

For both samples, their Q_{dl} values were much smaller than their Q_{ps} values, which was consistent with the Trasatti method analysis result and further verified that their capacitive behaviors were dominated by the pseudocapacitive mechanism. The Q_{ps} of the CeO_2/MnO_2–CFP electrode in dark was ~2.40×10^{-1} F, and it increased to ~2.78×10^{-1} F under visible light illumination, which represented an increase of ~16% from the photo-assisted charging effect. For the MnO_2–CFP electrode, its Q_{ps} increased from ~2.38×10^{-1} F in dark to ~2.55×10^{-1} F under visible light illumination, which represented an increase of only ~7% from the photo-assisted charging effect. These results were consistent with their CV curve and GCD behavior analysis results, which further confirmed that the decoration of a small amount of CeO_2 nanoparticles on the MnO_2–CFP electrode largely improved its photo-assisted charging capability.

3.8 Mechanism of long-lasting photo-induced capacitance enhancement in dark of the CeO_2/MnO_2–CFP sample

As shown in Fig. 3(e), the band structure of the CeO_2/MnO_2 heterojunction demonstrated that the CBM of MnO_2 (~1.22 V vs. NHE) was more positive than that of the Mn^{4+}/Mn^{3+} reduction potential (~0.95 V vs. NHE). So, the photo-generated electrons by MnO_2 under visible light illumination could not reduce Mn^{4+} to Mn^{3+} and then be stored there. Figure S6 in the ESM shows the high-resolution XPS scans over Mn 2p peaks of the MnO_2–CFP sample under visible light illumination and in dark after the illumination was switched off for 0.5 h, and they were compared with that in dark, as shown in Fig. S1(c) in the ESM. The Mn^{4+}:Mn^{3+} atomic ratios of the MnO_2–CFP sample were generally the same at ~71.1% : 28.9%, ~71.2% : 28.8%, and ~71.2% : 28.8% in dark, under visible light illumination, and in dark after the illumination, respectively, which demonstrated experimentally that no Mn^{4+} to Mn^{3+} reduction could happen under visible light illumination and was consistent with its band structure analysis result. Thus, the MnO_2–CFP electrode could not have the capability to retain part of its photo-induced capacitance enhancement after the illumination was switched off, as shown in Fig. S4 in the ESM.

For the CeO_2/MnO_2–CFP sample, however, the CBM of CeO_2 (~−0.49 V vs. NHE) was more negative than that of the Mn^{4+}/Mn^{3+} reduction potential (~0.95 V vs. NHE). So, part of the photo-generated electrons by CeO_2 under visible light illumination could transfer from CeO_2 to MnO_2 and be stored there by reducing Mn^{4+} to Mn^{3+}. Figure 8 shows the high-resolution XPS scans over Mn 2p peaks of the CeO_2/MnO_2–CFP sample under visible light illumination and in dark after the illumination was switched off for 0.5 h, and they were compared with that in dark, as shown in Fig. 2(b). The Mn^{4+}:Mn^{3+} atomic ratio of the CeO_2/MnO_2–

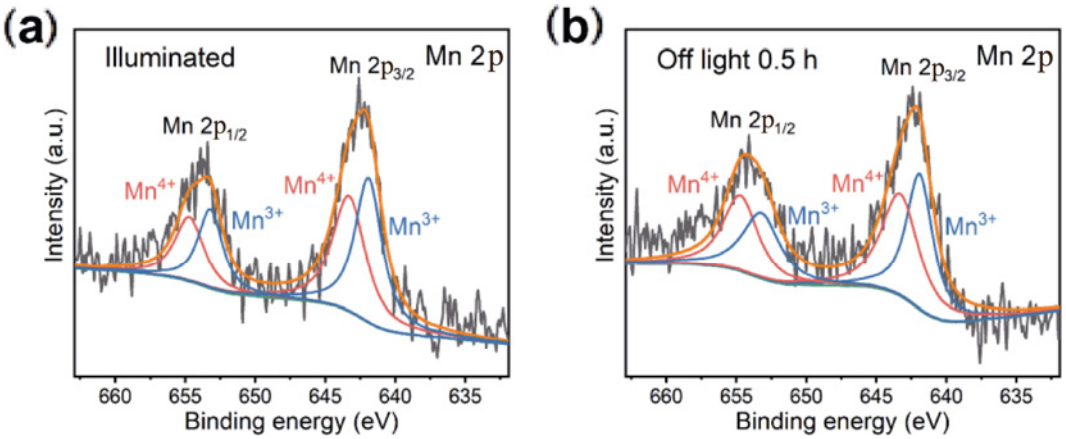

Fig. 8 High-resolution XPS scans over Mn 2p peaks of the CeO_2/MnO_2–CFP sample: (a) under visible light illumination and (b) in dark after the illumination was switched off for 0.5 h.

CFP sample decreased from ~58.0% : 42.0% in dark to ~49.2% : 50.8% under visible light illumination, which clearly verified that the reduction of Mn^{4+} to Mn^{3+} did happen in the CeO_2/MnO_2–CFP sample upon visible light illumination, as its band structure analysis result predicted. After the illumination was switched off for 0.5 h, its Mn^{4+}:Mn^{3+} atomic ratio only increased to ~51.7% : 48.3%, which suggested that most stored electrons were not released immediately in dark after the illumination was switched off. Thus, the CeO_2/MnO_2–CFP sample could have the desired capability to retain a large part of its capacitance enhancement by the photo-assisted charging in dark for an extended period of time. Because the Mn^{4+}/Mn^{3+} reduction potential (~0.95 V vs. NHE) was more positive than both the one-electron reduction potential of O_2 (−0.05 V vs. NHE) and the two-electron reduction potential of O_2 (0.68 V vs. NHE), those stored photo-generated electrons from the reduction of Mn^{4+} to Mn^{3+} could not release in dark by reducing O_2, as happened from the normal photocatalytic memory effect [73–76]. Thus, their release in dark could be largely slowed down. Even after 12 h in dark, ~56% of its capacitance enhancement from the photo-charging was still retained, which was far higher than that in Ref. [77] on the h-WO_3/Bi_2WO_6 material system (16% retainment after only 5 h in dark) from the photocatalytic memory effect. To create photo-generated electron storage by reducing Mn^{4+} to Mn^{3+} with the proper Mn^{4+}/Mn^{3+} reduction potential successfully avoided their reaction with O_2, which largely slowed down their release and was critical for the observed long-lasting photo-assisted capacitance enhancement of the CeO_2/MnO_2–CFP electrode in dark.

4 Conclusions

In summary, a two-step *in-situ* growth approach was developed to create a composite system of CeO_2/MnO_2–CFP, which could serve as a binder-free electrode for supercapacitors. The CFP support could allow the rapid electrolyte diffusion through the hollow/open framework and the fast electron transfer though the carbon skeleton, while the elimination of binders could further enhance its conductivity and stability. The electrochemical energy storage of the CeO_2/MnO_2–CFP electrode was found to be dominated by the pseudocapacitive mechanism. The decoration of a small amount of CeO_2 nanoparticles significantly enhances its photo-assisted charging capability, which could be attributed to the formation of a type II CeO_2/MnO_2 heterojunction to largely enhance the separation and transfer of photo-generated charge carriers for their participation in the photo-assisted charging process. For example, the photo-assisted charging increased its specific capacitance relatively steadily for ~41–49 $F \cdot g^{-1}$ when the charging and discharging current densities were from 0.25 to 2.5 $A \cdot g^{-1}$, while that of the MnO_2–CFP electrode without CeO_2 decoration was only ~10–20 $F \cdot g^{-1}$. Furthermore, the CeO_2/MnO_2–CFP electrode possessed a superior retainment effect on its photo-enhanced capacity in dark for an extended period of time, which could be attributed to its slow release of stored photo-generated charges due to the more positive potential of Mn^{4+}/Mn^{3+} than the one- and two-electron reduction potentials of O_2. Even after the visible light illumination was shut off for 12 h, it still retained over half of its photo-enhanced capacity. By optimizing the CeO_2/MnO_2 mass ratio, sizes and shapes

of CeO_2 and MnO_2 nanostructures, and the atomic ratio of Mn^{3+}/Mn^{4+}, the photo-assisted charging capability and its retainment in dark of the CeO_2/MnO_2–CFP electrode could be further enhanced. This study provided the principles on the design of supercapacitors with both the photo-assisted charging capability and its retainment in dark for an extended period of time, which could be readily applied on various pseudocapacitive material systems to advance the development of solar energy utilization devices.

Acknowledgements

This study was supported by the National Natural Science Foundation of China (Grant No. 51902271), the Fundamental Research Funds for the Central Universities (Grant Nos. 2682021CX116, 2682020CX07, and 2682020CX08), and Sichuan Science and Technology Program (Grant Nos. 2020YJ0259, 2020YJ0072, and 2021YFH0163). We would like to thank Analysis and Testing Center of Southwest Jiaotong University for the assistance on material characterization.

Electronic Supplementary Material

Supplementary material is available in the online version of this article at https://doi.org/10.1007/s40145-022-0644-9.

References

[1] Chu S, Cui Y, Liu N. The path towards sustainable energy. *Nat Mater* 2017, **16**: 16–22.

[2] Liu WJ, Jiang H, Yu HQ. Emerging applications of biochar-based materials for energy storage and conversion. *Energy Environ Sci* 2019, **12**: 1751–1779.

[3] Chu S, Majumdar A. Opportunities and challenges for a sustainable energy future. *Nature* 2012, **488**: 294–303.

[4] Gurung A, Qiao QQ. Solar charging batteries: Advances, challenges, and opportunities. *Joule* 2018, **2**: 1217–1230.

[5] Kabir E, Kumar P, Kumar S, *et al*. Solar energy: Potential and future prospects. *Renew Sustain Energy Rev* 2018, **82**: 894–900.

[6] Armaroli N, Balzani V. The future of energy supply: Challenges and opportunities. *Angew Chem Int Ed* 2007, **46**: 52–66.

[7] Yang M, Wang P, Li YJ, *et al*. Graphene aerogel-based NiAl-LDH/g-C_3N_4 with ultratight sheet–sheet heterojunction for excellent visible-light photocatalytic activity of CO_2 reduction. *Appl Catal B Environ* 2022, **306**: 121065.

[8] Gao RQ, He H, Bao JX, *et al*. Pyrene–benzothiadiazole-based polymer/CdS 2D/2D organic/inorganic hybrid S-scheme heterojunction for efficient photocatalytic H_2 evolution. *Chin J Struct Chem* 2022, **41**: 2206031–2206038.

[9] Han GW, Xu FY, Cheng B, *et al*. Enhanced photocatalytic H_2O_2 production over inverse opal ZnO@polydopamine S-scheme heterojunctions. *Acta Phys-Chim Sin* 2022, **38**: 2112037.

[10] Schmidt D, Hager MD, Schubert US. Photo-rechargeable electric energy storage systems. *Adv Energy Mater* 2016, **6**: 1500369.

[11] Lethien C, le Bideau J, Brousse T. Challenges and prospects of 3D micro-supercapacitors for powering the internet of things. *Energy Environ Sci* 2019, **12**: 96–115.

[12] Miller JR, Simon P. Electrochemical capacitors for energy management. *Science* 2008, **321**: 651–652.

[13] Simon P, Gogotsi Y. Materials for electrochemical capacitors. *Nat Mater* 2008, **7**: 845–854.

[14] Shao YL, El-Kady MF, Sun JY, *et al*. Design and mechanisms of asymmetric supercapacitors. *Chem Rev* 2018, **118**: 9233–9280.

[15] Choudhary N, Li C, Moore J, *et al*. Asymmetric supercapacitor electrodes and devices. *Adv Mater* 2017, **29**: 1605336.

[16] Boruah BD, Mathieson A, Wen B, *et al*. Photo-rechargeable zinc-ion capacitor using 2D graphitic carbon nitride. *Nano Lett* 2020, **20**: 5967–5974.

[17] Boruah BD, Wen B, Nagane S, *et al*. Photo-rechargeable zinc-ion capacitors using V_2O_5-activated carbon electrodes. *ACS Energy Lett* 2020, **5**: 3132–3139.

[18] Bai L, Huang H, Zhang S, *et al*. Photocatalysis-assisted Co_3O_4/g-C_3N_4 p–n junction all-solid-state supercapacitors: A bridge between energy storage and photocatalysis. *Adv Sci* 2020, **7**: 2001939.

[19] Zhu KJ, Zhu GX, Wang J, *et al*. Direct storage of holes in ultrathin $Ni(OH)_2$ on Fe_2O_3 photoelectrodes for integrated solar charging battery-type supercapacitors. *J Mater Chem A* 2018, **6**: 21360–21367.

[20] Wang H, Cao J, Zhou Y, *et al*. Carbon dot-modified mesoporous carbon as a supercapacitor with enhanced light-assisted capacitance. *Nanoscale* 2020, **12**: 17925–17930.

[21] Zhu MS, Huang Y, Huang Y, *et al*. Capacitance enhancement in a semiconductor nanostructure-based supercapacitor by solar light and a self-powered supercapacitor–photodetector system. *Adv Funct Mater* 2016, **26**: 4481–4490.

[22] Ren Y, Zhu T, Liu Y, *et al*. Direct utilization of photoinduced charge carriers to promote electrochemical energy storage. *Small* 2021, **17**: e2008047.

[23] Boruah BD, Mathieson A, Park SK, *et al*. Vanadium dioxide cathodes for high-rate photo-rechargeable zinc-ion batteries. *Adv Energy Mater* 2021, **11**: 2100115.

[24] Li HJ, Wang MM, Qi GH, *et al*. Oriented bacteriorhodopsin/polyaniline hybrid bio-nanofilms as photo-assisted electrodes for high performance supercapacitors. *J Mater Chem A* 2020, **8**: 8268–8272.

[25] Boruah BD, Mathieson A, Wen B, *et al*. Photo-rechargeable zinc-ion batteries. *Energy Environ Sci* 2020, **13**: 2414–2421.

[26] An CH, Wang ZF, Xi W, *et al*. Nanoporous Cu@Cu_2O

hybrid arrays enable photo-assisted supercapacitor with enhanced capacities. *J Mater Chem A* 2019, 7: 15691–15697.

[27] Mohammadian M, Rashid-Nadimi S, Peimanifard Z. Fluorine-doped tin oxide/hematite/$Ni(OH)_2$/prussian white photoelectrode for use in a visible-light-assisted pseudocapacitor. *J Power Sources* 2019, **426**: 40–46.

[28] Ma ZP, Shao GJ, Fan YQ, *et al*. Construction of hierarchical α-MnO_2 nanowires@ultrathin δ-MnO_2 nanosheets core–shell nanostructure with excellent cycling stability for high-power asymmetric supercapacitor electrodes. *ACS Appl Mater Interfaces* 2016, **8**: 9050–9058.

[29] Wang JG, Kang FY, Wei BQ. Engineering of MnO_2-based nanocomposites for high-performance supercapacitors. *Prog Mater Sci* 2015, **74**: 51–124.

[30] Lv ZS, Luo YF, Tang YX, *et al*. Editable supercapacitors with customizable stretchability based on mechanically strengthened ultralong MnO_2 nanowire composite. *Adv Mater* 2018, **30**: 1704531.

[31] Peng P, Deng YJ, Niu JP, *et al*. Fabrication and electrical characteristics of flash-sintered SiO_2-doped ZnO–Bi_2O_3–MnO_2 varistors. *J Adv Ceram* 2020, **9**: 683–692.

[32] Zhao PY, Cai ZM, Wu LW, *et al*. Perspectives and challenges for lead-free energy-storage multilayer ceramic capacitors. *J Adv Ceram* 2021, **10**: 1153–1193.

[33] Li DX, Zeng XJ, Li ZP, *et al*. Progress and perspectives in dielectric energy storage ceramics. *J Adv Ceram* 2021, **10**: 675–703.

[34] Yang R, Fan Y, Ye R, *et al*. MnO_2-based materials for environmental applications. *Adv Mater* 2021, **33**: e2004862.

[35] Guo W, Yu C, Li SF, *et al*. Strategies and insights towards the intrinsic capacitive properties of MnO_2 for supercapacitors: Challenges and perspectives. *Nano Energy* 2019, **57**: 459–472.

[36] Ma R, Zhang S, Wen T, *et al*. A critical review on visible-light-response CeO_2-based photocatalysts with enhanced photooxidation of organic pollutants. *Catal Today* 2019, **335**: 20–30.

[37] Liang MF, Borjigin T, Zhang YH, *et al*. Controlled assemble of hollow heterostructured g-C_3N_4@CeO_2 with rich oxygen vacancies for enhanced photocatalytic CO_2 reduction. *Appl Catal B Environ* 2019, **243**: 566–575.

[38] Wang Z, Yu R. Hollow micro/nanostructured ceria-based materials: Synthetic strategies and versatile applications. *Adv Mater* 2019, **31**: e1800592.

[39] Cao C, Xie J, Zhang SC, *et al*. Graphene-like δ-MnO_2 decorated with ultrafine CeO_2 as a highly efficient catalyst for long-life lithium–oxygen batteries. *J Mater Chem A* 2017, **5**: 6747–6755.

[40] Wang JD, Xiao X, Liu Y, *et al*. The application of CeO_2-based materials in electrocatalysis. *J Mater Chem A* 2019, **7**: 17675–17702.

[41] Mofarah SS, Adabifiroozjaei E, Yao Y, *et al*. Proton-assisted creation of controllable volumetric oxygen vacancies in ultrathin CeO_{2-x} for pseudocapacitive energy storage applications. *Nat Commun* 2019, **10**: 2594.

[42] Gong HM, Li YJ, Li HY, *et al*. 2D CeO_2 and a partially phosphated 2D Ni-based metal–organic framework formed an S-scheme heterojunction for efficient photocatalytic hydrogen evolution. *Langmuir* 2022, **38**: 2117–2131.

[43] Guo D, Yu XZ, Shi W, *et al*. Facile synthesis of well-ordered manganese oxide nanosheet arrays on carbon cloth for high-performance supercapacitors. *J Mater Chem A* 2014, **2**: 8833–8838.

[44] Xu ZH, Sun SS, Cui W, *et al*. Interconnected network of ultrafine MnO_2 nanowires on carbon cloth with weed-like morphology for high-performance supercapacitor electrodes. *Electrochimica Acta* 2018, **268**: 340–346.

[45] Luo YS, Jiang J, Zhou WW, *et al*. Self-assembly of well-ordered whisker-like manganese oxide arrays on carbon fiber paper and its application as electrode material for supercapacitors. *J Mater Chem* 2012, **22**: 8634–8640.

[46] Guo S, Sun WZ, Yang WY, *et al*. Synthesis of Mn_3O_4/CeO_2 hybrid nanotubes and their spontaneous formation of a paper-like, free-standing membrane for the removal of arsenite from water. *ACS Appl Mater Interfaces* 2015, **7**: 26291–26300.

[47] Chong SK, Wu YF, Liu CF, *et al*. Cryptomelane-type MnO_2/carbon nanotube hybrids as bifunctional electrode material for high capacity potassium-ion full batteries. *Nano Energy* 2018, **54**: 106–115.

[48] Liu T, Jiang CJ, You W, *et al*. Hierarchical porous C/MnO_2 composite hollow microspheres with enhanced supercapacitor performance. *J Mater Chem A* 2017, **5**: 8635–8643.

[49] Wu P, Dai SQ, Chen GX, *et al*. Interfacial effects in hierarchically porous α-MnO_2/Mn_3O_4 heterostructures promote photocatalytic oxidation activity. *Appl Catal B Environ* 2020, **268**: 118418.

[50] Jabeen N, Xia QY, Savilov SV, *et al*. Enhanced pseudocapacitive performance of α-MnO_2 by cation preinsertion. *ACS Appl Mater Interfaces* 2016, **8**: 33732–33740.

[51] Kumar M, Yun JH, Bhatt V, *et al*. Role of Ce^{3+} valence state and surface oxygen vacancies on enhanced electrochemical performance of single step solvothermally synthesized CeO_2 nanoparticles. *Electrochimica Acta* 2018, **284**: 709–720.

[52] Huang XB, Zhao GX, Chang YQ, *et al*. Nanocrystalline $CeO_{2-\delta}$ coated β-MnO_2 nanorods with enhanced oxygen transfer property. *Appl Surf Sci* 2018, **440**: 20–28.

[53] Feng NJ, Zhu ZJ, Zhao P, *et al*. Facile fabrication of trepang-like CeO_2@MnO_2 nanocomposite with high catalytic activity for soot removal. *Appl Surf Sci* 2020, **515**: 146013.

[54] Zhao JH, Nan J, Zhao ZW, *et al*. Energy-efficient fabrication of a novel multivalence Mn_3O_4–MnO_2 heterojunction for dye degradation under visible light irradiation. *Appl Catal B Environ* 2017, **202**: 509–517.

[55] Loyalka SK, Riggs CA. Inverse problem in diffuse reflectance spectroscopy: Accuracy of the Kubelka–Munk equations. *Appl Spectrosc* 1995, **49**: 1107–1110.

[56] Tauc J, Grigorovici R, Vancu A. Optical properties and

electronic structure of amorphous germanium. *Phys Status Solidi B* 1966, **15**: 627–637.

[57] Wang M, Shen M, Zhang LX, *et al*. 2D–2D MnO_2/g-C_3N_4 heterojunction photocatalyst: *In-situ* synthesis and enhanced CO_2 reduction activity. *Carbon* 2017, **120**: 23–31.

[58] Barreca D, Gri F, Gasparotto A, *et al*. Multi-functional MnO_2 nanomaterials for photo-activated applications by a plasma-assisted fabrication route. *Nanoscale* 2018, **11**: 98–108.

[59] Mo Z, Xu H, Chen ZG, *et al*. Construction of MnO_2/Monolayer g-C_3N_4 with Mn vacancies for Z-scheme overall water splitting. *Appl Catal B Environ* 2019, **241**: 452–460.

[60] Wen XJ, Niu CG, Zhang L, *et al*. A novel Ag_2O/CeO_2 heterojunction photocatalysts for photocatalytic degradation of enrofloxacin: Possible degradation pathways, mineralization activity and an in depth mechanism insight. *Appl Catal B Environ* 2018, **221**: 701–714.

[61] Ko JW, Kim JH, Park CB. Synthesis of visible light-active CeO_2 sheets via mussel-inspired $CaCO_3$ mineralization. *J Mater Chem A* 2013, **1**: 241–245.

[62] Chen SS, Qi Y, Liu GJ, *et al*. A wide visible-light-responsive tunneled $MgTa_2O_{6-x}N_x$ photocatalyst for water oxidation and reduction. *Chem Commun* 2014, **50**: 14415–14417.

[63] Yan PC, Mo Z, Dong JT, *et al*. Construction of Mn valence-engineered MnO_2/BiOCl heterojunction coupled with carriers-trapping effect for enhanced photoelectrochemical lincomycin aptasensor. *Sens Actuat B Chem* 2020, **320**: 128415.

[64] Ghasemian MB, Mayyas M, Idrus-Saidi SA, *et al*. Self-limiting galvanic growth of MnO_2 monolayers on a liquid metal−Applied to photocatalysis. *Adv Funct Mater* 2019, **29**: 1901649.

[65] Hong XD, Li Y, Wang X, *et al*. Carbon nanosheet/MnO_2/BiOCl ternary composite for degradation of organic pollutants. *J Alloys Compd* 2022, **891**: 162090.

[66] Wu BK, Zhang GB, Yan MY, *et al*. Graphene scroll-coated α-MnO_2 nanowires as high-performance cathode materials for aqueous Zn-ion battery. *Small* 2018, **14**: e1703850.

[67] Li Q, Dai ZW, Wu JB, *et al*. Fabrication of ordered macro-microporous single-crystalline MOF and its derivative carbon material for supercapacitor. *Adv Energy Mater* 2020, **10**: 1903750.

[68] Wang Y, Song Y, Xia Y. Electrochemical capacitors: Mechanism, materials, systems, characterization and applications. *Chem Soc Rev* 2016, **45**: 5925–5950.

[69] Ardizzone S, Fregonara G, Trasatti S. "Inner" and "outer" active surface of RuO_2 electrodes. *Electrochimica Acta* 1990, **35**: 263–267.

[70] Baronetto D, Krstajić N, Trasatti S. Reply to "note on a method to interrelate inner and outer electrode areas" by H. Vogt. *Electrochimica Acta* 1994, **39**: 2359–2362.

[71] Zhu MS, Meng WJ, Huang Y, *et al*. Proton-insertion-enhanced pseudocapacitance based on the assembly structure of tungsten oxide. *ACS Appl Mater Interfaces* 2014, **6**: 18901–18910.

[72] Boruah BD, Wen B, de Volder M. Light rechargeable lithium-ion batteries using V_2O_5 cathodes. *Nano Lett* 2021, **21**: 3527–3532.

[73] Li Q, Li YW, Wu PG, *et al*. Palladium oxide nanoparticles on nitrogen-doped titanium oxide: Accelerated photocatalytic disinfection and post-illumination catalytic "memory". *Adv Mater* 2008, **20**: 3717–3723.

[74] Li Q, Li YW, Liu ZQ, *et al*. Memory antibacterial effect from photoelectron transfer between nanoparticles and visible light photocatalyst. *J Mater Chem* 2010, **20**: 1068–1072.

[75] Feng F, Yang WY, Gao S, *et al*. Postillumination activity in a single-phase photocatalyst of Mo-doped TiO_2 nanotube array from its photocatalytic "memory". *ACS Sustain Chem Eng* 2018, **6**: 6166–6174.

[76] Yang WY, Chen Y, Gao S, *et al*. Post-illumination activity of Bi_2WO_6 in the dark from the photocatalytic "memory" effect. *J Adv Ceram* 2021, **10**: 355–367.

[77] Ma HQ, Yang WY, Gao S, *et al*. Photoirradiation-induced capacitance enhancement in the h-WO_3/Bi_2WO_6 submicron rod heterostructure under simulated solar illumination and its postillumination capacitance enhancement retainment from a photocatalytic memory effect. *ACS Appl Mater Interfaces* 2021, **13**: 57214–57229.